Journal of Biomechanical Engineering. Received March 18, 2019;
Accepted manuscript posted October 2, 2019. doi:10.1115/1.4045050

Ultrasound imaging characterization of soft tissue dynamics of the seated human body

Daisuke Yamada
Senior principal engineer
Toyota Research Institute North America
1555 Woodridge avenue,
Ann Arbor, MI 48105
Visiting research fellow
John A. Paulson School of
Engineering and Applied Sciences
Harvard University
60 Oxford street,
Cambridge, MA 02138
Email: dyamada@seas.harvard.edu

Alperen Değirmenci
Graduate student
John A. Paulson School of
Engineering and Applied Sciences
Harvard University
60 Oxford street,
Cambridge, MA 02138
Email: adegirmenci@seas.harvard.edu

Robert D. Howe
Abbott and James Lawrence Professor of Engineering
John A. Paulson School of Engineering and Applied Sciences
Harvard University
323 Pierce Hall, 29 Oxford street, Cambridge, MA 02138
Email: howe@seas.harvard.edu

ABSTRACT

To characterize the dynamics of internal soft organs and external anatomical structures, this paper presents a system that combines medical ultrasound imaging with an optical tracker and a vertical exciter that imparts whole-body vibrations on seated subjects. The spatial and temporal accuracy of the system was validated using a phantom with calibrated internal structures, resulting in 0.224 mm maximum root mean square (r.m.s.) position error and 13 ms maximum synchronization error between sensors. In addition to the dynamics of the head and sternum, stomach dynamics were characterized by extracting the centroid of the stomach from the ultrasound images. The system was used to characterize the subject-specific body dynamics as well as the intra-subject variabilities caused by excitation pattern (frequency up-sweep, down-sweep, and white noise, 1 to 10 Hz), excitation amplitude (1 and 2 m/s^2 r.m.s.), seat compliance (rigid and soft), and stomach filling (empty and 500 mL water). Human subjects experiments (n = 3) yielded preliminary results for

the frequency response of the head, sternum, and stomach. The method presented here provides the first detailed in vivo characterization of internal and external human body dynamics. Tissue dynamics characterized by the system can inform design of vehicle structures and adaptive control of seat and suspension systems, as well as validate finite element models for predicting passenger comfort in the early stages of vehicle design.

NOMENCLATURE

$\boldsymbol{d}^a_{part}$ Position vector from the origin point of the absolute coordinate system to the part indicated as *part*.

$\boldsymbol{d}^c_{part}$ Position vector from the origin point of the camera coordinate system to the part indicated as *part*.

$\boldsymbol{d}^i_{part}$ Position vector from the origin point of the image plane coordinate system to the point of interest indicated as *part*.

$\boldsymbol{T}^y_x$ Homogeneous transformation matrix from coordinate system x to y.

$F_{part,Z}$ Transfer function of the part indicated as *part* about Z-axis direction which is the vertical direction in the absolute coordinate system.

$F_{part,X}$ Transfer function of the part indicated as *part* about X-axis direction which is the fore-and-aft direction in the absolute coordinate system.

$D^a_{part,Z}$ Fourier transformed Z-axis component of the time series of $\boldsymbol{d}^a_{part}$.

$D^a_{part,X}$ Fourier transformed X-axis component of the time series of $\boldsymbol{d}^a_{part}$.

$D^a_{ve,Z}$ Fourier transformed Z-axis component of the time series of $\boldsymbol{d}^a_{ve}$ which is the position vector from the origin point of the absolute coordinate system to the reflective marker affixed to the vibration exciter.

ω frequency.

$A(q)$ Coefficient of the auto-regressive exogeneous model.

$B(q)$ Coefficient of the auto-regressive exogeneous model.

q Delay operator.

a_p Coefficient in $A(q)$ corresponding to term of q whose power is -p.

b_p Coefficient in $B(q)$ corresponding to term of q whose power is -p.

n_a Number of poles.

n_b Number of zeros.

$\bar{F}(s)$ Continuous-time system model.

$A(s)$ Denominator of $\bar{F}(s)$.

$B(s)$ Numerator of $\bar{F}(s)$.

s Laplace variable.

J Cost function to be minimized for obtaining optimal $A(s)$ and $B(s)$.

$\hat{F}(\omega)$ Frequency response function of $\bar{F}(s)$.

1 INTRODUCTION

1.1 Motivation

Understanding body dynamics can enable better design of products that people drive, ride, or wear. Measuring the mechanical response of the body to mechanical stimuli and modeling the body as a mechanical transmission system enables predicting the relationship between imparted forces and resulting motions of organs and structures, which can reveal the mechanical properties of these tissues. In addition, developing methods to measure physical response enables studying the physiological effects generated by these mechanical interactions. For instance, motion sickness during passive locomotion in vehicles is caused by body accelerations that the person has not adapted to [1]. One of the essential causes of the motion sickness is an inter-sensory conflict between vestibular, visual, and somatosensory stimuli [2]. Since mechanoreceptors for somatosensory nerves are embedded in soft tissue, study of the dynamic response of internal soft tissues can provide a better understanding of both physical and mental phenomena caused by mechanical stimulation.

1.2 Previous Studies

Both experimental and analytical methods have been used in prior studies of body dynamics. Most experimental studies have used accelerometers to observe the dynamic response of each body part to imparted vibrations. For example, to simultaneously identify the translational and rotational responses of the head, dynamic response was measured with a bite bar containing multiple accelerometers that was held between the subject's teeth [3]. Through analysis of such data, the apparent mass of the seated human as well as the transmissibility of the vibration from the seat to various body parts have been characterized as frequency response functions [4–13]. In addition, cross-axis responses [4–9], posture dependency [4,6,9–11], muscle tone dependency [4,8,11], excitation pattern dependency [5,8], and nonlinear response [5–8, 11–13] have been characterized. Subjective evaluation of whole-body vibration has examined relative tolerance of vibration magnitude [14], discomfort level [15–18], and low back pain [19].

These studies have focused only on the dynamic responses that can be observed at the skin surface. In

contrast, Coermann proposed an experimental method to characterize the internal and external dynamics of the thorax-abdomen subsystem [20]. The dynamic response to longitudinal vibration in the supine position was characterized by measuring abdominal wall displacements, chest circumference and air flow through the mouth based on an assumption that the motion of the abdominal viscera caused the change of the three physical values. The method provided a general view of the dynamics of internal structures of the body, but the behavior of specific soft tissue structures have yet to be clarified.

Physical modeling of body dynamics has included lumped-mass [21], multi-body dynamics [22–26], and finite element models [27] to characterize the frequency response of the seated human body. The dynamics of the head-spine-pelvis skeletal system was the primary target in previous studies, however Tamaoki [23] and Matsumoto [24] showed that introducing the abdominal viscera improves the fitting quality of the skin surface frequency response functions. The response of the abdominal viscera was not validated in these studies, but the authors suggested that dynamic response of the internal soft tissue played an important role in overall body dynamics.

1.3 Research approach

To address the lack of direct measurements of internal soft tissue dynamics, this paper presents a system to measure the behavior of internal and external body structures under whole-body vibrations. The system comprises an ultrasound imaging system, an optical tracker, and a whole-body vibration exciter, and can be used to identify the dynamic characteristics of soft tissue as a frequency response function. Due to its compact form, low cost, and high sampling rate, medical ultrasound imaging is used to measure the *in vivo* dynamic motion and deformation of internal soft tissues. The optical tracker is used both to track the dynamic responses at the skin surface and to compensate for the vibration-induced motion of the ultrasound probe. In addition to details of the system design and validation, this paper presents preliminary results that illustrate the type of data that can be obtained with this approach. This includes frequency response of the stomach compared with the dynamics of the head and sternum, as well as a limited assessment of intra- and inter-subject variability under a variety of conditions.

2 SYSTEM DESIGN AND VALIDATION

2.1 System Configuration

The system consists of an ultrasound imaging machine, an optical tracker, and a vibration exciter (Fig. 1). The ultrasound imaging machine (Sonos 7500, Philips Healthcare, Andover, MA, USA) was used

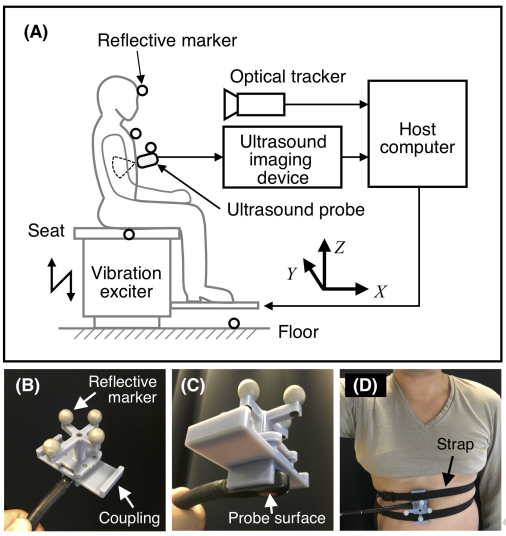

Fig. 1. System configuration.(A)Overall configuration, (B, C)Assembly of the TEE probe, the reflective markers, and the coupling, (D)Affixed TEE probe using two straps.

to image soft tissue at 30 Hz. A transesophageal echocardiography (TEE) ultrasound probe (Omni III, Philips Healthcare, Andover, MA, USA) was affixed to the surface of the subject's body using two straps through a 3D-printed coupling. The TEE probe was chosen for its low profile, reducing inertial loads that can cause the probe to move during excitation, as well as the ability to mechanically rotate the ultrasound imaging plane to select a viewing plane. An actuated seat system (ClearMotion Active Suspension Seat, ClearMotion Inc., Woburn, MA, USA), which was originally developed for heavy-duty truck drivers to reduce bodily vibration by counteracting external disturbances, was repurposed as a vibration exciter. Its powerful electromagnetic actuator lends itself well to generating input vibrations that mimic road conditions.

A high-precision optical tracker (fusionTrack 500, AtracSys GmbH, Switzerland) was used to track reflective markers at a sampling rate of 333 Hz and accuracy of 90 μm. Sets of four markers at each location enabled tracking of both position and orientation. The passive motion of the ultrasound probe, the skin surface responses at several parts of the anatomy, the vertical seat motion, and a fixed ground location were tracked.

2.2 Dynamic response measurement

The optical tracker identified the instantaneous position and rotation matrix of the body part coordinate system with respect to the camera coordinate system (Fig. 2). The tracker marker set affixed to the floor defined the absolute coordinate system, and the position of each part with respect to the absolute coordinate

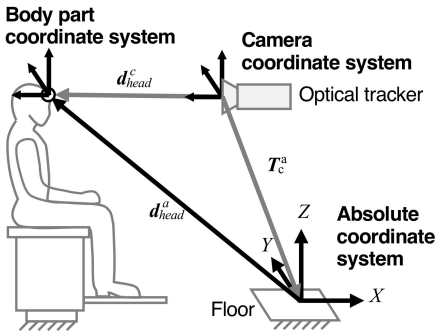

Fig. 2. Coordinate transforms for resolving body part motions to the absolute fixed coordinate system, using head motion as an example.

system $\boldsymbol{d}^a_{part}$ could be calculated as

$$\boldsymbol{d}^a_{part} = (\boldsymbol{T}^a_c)^{-1}\boldsymbol{d}^c_{part} \tag{1}$$

where $\boldsymbol{d}^c_{part}$ is the position vector and $\boldsymbol{T}^a_c$ is the homogeneous transformation matrix from the camera coordinate system to the absolute coordinate system.

To track the dynamic response of internal soft tissue structures, tissue motion must be extracted from the ultrasound images. This process can be optimized for each tissue structure type [28, 29]; here we present an image processing pipeline to find the centroid of the stomach as an example (Fig. 3).

Stomach, liver, and abdominal muscles can be seen in the raw ultrasound image. The abdominal muscles are recognized as a thick layer separated from other internal organs with a bright curve. The stomach was observed as a dark hollow area surrounded by a bright ellipsoidal perimeter. First, the raw ultrasound image was denoised using a Gaussian filter. Second, the perimeter of the stomach was extracted using an active contour model [30, 31]. Finally, the centroid of the stomach was determined as the geometrical center of the delineated area.

The point of interest in the image plane coordinate system was then transformed into the absolute coordinate system (Fig. 4). The marker set affixed to the ultrasound probe defined the ultrasound probe coordinate system. The homogeneous transformation $\boldsymbol{T}^i_p$ between the ultrasound probe coordinate system and the image plane coordinate system was calibrated using the algorithm in the Public software Library for

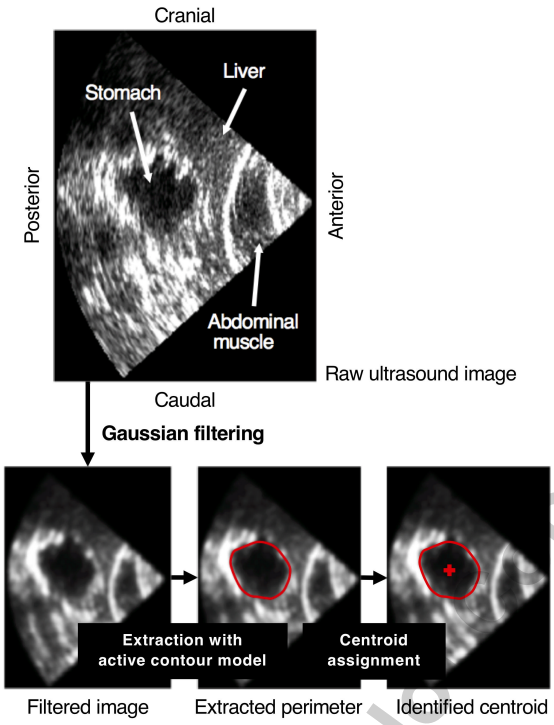

Fig. 3. Image processing pipeline for extracting the stomach centroid.

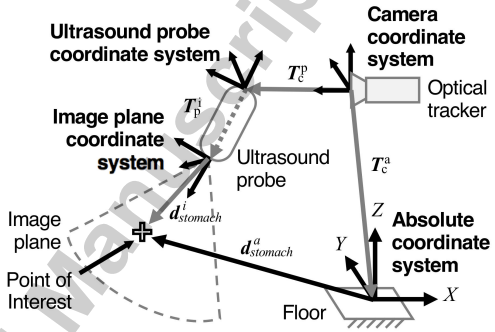

Fig. 4. Coordinate transforms for resolving the stomach centroid into absolute coordinates.

UltraSound (PLUS) Toolkit [32]. The stomach centroid in absolute coordinates $\boldsymbol{d}^a_{part}$ is then calculated as

$$\boldsymbol{d}^a_{part} = (\boldsymbol{T}^a_c)^{-1}\boldsymbol{T}^p_c\boldsymbol{T}^i_p\boldsymbol{d}^i_{part} \tag{2}$$

where $\boldsymbol{d}^i_{part}$ is the point of interest in the ultrasound image with respect to the image plane coordinate system and $\boldsymbol{T}^p_c$ is the homogeneous transformation from the camera coordinate system to the ultrasound

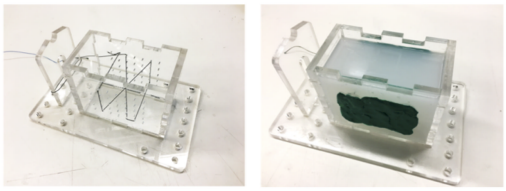

(a) Outer structure (b) Filled with silicone rubber

Fig. 5. String-based phantom for testing system accuracy. Strings are mounted at skew angles so inter-string distances as measured in the ultrasound images define unique image plane locations and orientations in phantom coordinates, following standard ultrasound calibration methods [32].

probe coordinates.

2.3 Validation

2.3.1 Methods

System validation must account for two sources of error in the position measurement process: errors in the optical tracker, and errors due to resolving positions in the ultrasound images into optical tracker coordinates. Optical tracking is a mature technology and a number of studies have carefully characterized accuracy (e.g. [33–35]). Xiao et al. [36] evaluated the accuracy of the tracker used here (AtracSys fusionTrack 500) under conditions similar to those used in this study, and found the root mean square (r.m.s.) position error was 0.240 mm for the displacement magnitudes used here.

The spatial accuracy of resolving positions in the ultrasound images into optical tracking coordinates was assessed using a string-based ultrasound phantom, where known string locations could be compared to image-derived locations (Fig. 5). Three strings were precisely positioned in the laser-cut phantom housing, which was then filled with silicone rubber (Ecoflex 00-50, Smooth-On Inc., PA, USA) to enable ultrasound imaging. The phantom was mounted on the vibration exciter, and reflective markers were affixed to the outer structure of the phantom to define the phantom coordinate system. The location of the embedded strings was fixed in the phantom coordinate system while undergoing vibration due to the stiffness of the silicone rubber. The TEE probe with optical tracking markers was placed on the surface of the phantom to image the strings locations, and frequency-sweep vibration (1 to 10 Hz over 20 sec) at 1 m/s^2 r.m.s. amplitude was applied to the phantom.

The positions of the embedded phantom strings were measured by the image-based method in Section 2.2 above. String locations, which appear as minuscule dots in the images, were manually selected, then their locations were transformed to absolute coordinates using Eq. 2. Reference values for the string locations in optical tracker coordinates were calculated using the CAD model from which the phantom was

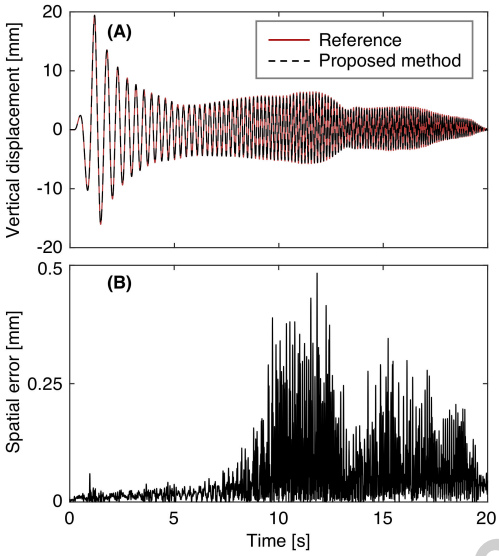

Fig. 6. Validation result. (A)Vertical displacement of the reference and the cross point, (B) Spatial error.

constructed, which included the marker locations. Spatial accuracy was evaluated by comparing the frame-by-frame displacements of the image-based method to the reference values.

Ultrasound images and optical tracker data were recorded separately during the experiment, so temporal synchronization was also characterized. The ultrasound probe was affixed to the string-based phantom and sharply tapped six times at one-minute intervals as images and data were continuously recorded. The motion caused by tapping could be precisely identified both in the ultrasound images and in the trajectory of the ultrasound probe measured with the optical tracker. Relative temporal accuracy was evaluated by comparing the time gaps between taps derived from the image and data timestamps.

2.4 Validation results

Figure 6 compares typical vertical motion trajectories for one string position derived from the ultrasound image with the reference position based on the phantom geometry. The root mean square errors between the three cross point coordinates measured with the two different methods were 0.224 mm, 0.211 mm, and 0.147 mm, respectively.

The mean absolute error of the time gaps obtained from the experiment for clarifying the temporal synchronization was 13 ms, which is directly attributable to the difference in sampling rates (30 Hz for the images and 333 Hz for the optical tracker).

Previous studies have shown that the first order natural frequency of the seated human body can be around 5 Hz [8, 11]. The amplitude of a sinusoidal wave at 5 Hz and 1 m/s^2 r.m.s. acceleration is 1.4 mm.

Table 1. Order of the trials.

Order	Seat	Stomach	Iteration
1-6			1st
7-12	Rigid	Empty	2nd
13-18			3rd
19-24			1st
25-30	Soft	Empty	2nd
31-36			3rd
Subjects were asked to drink 500 mL of water.			
37-42			1st
43-48	Soft	Filled	2nd
49-54			3rd
55-60			1st
61-66	Rigid	Filled	2nd
67-72			3rd

Table 2. Information about the experimental subjects.

Subject	1	2	3
Gender	Male	Male	Male
Age	39	27	38
Height	1.70 m	1.68 m	1.81 m
Weight	70 kg	70 kg	62 kg
BMI	24.2	24.8	18.9

Considering that the physical response at the resonance can be amplified, the maximum root mean square error of 0.224 mm is acceptable. 13 ms is equivalent to 0.4 rad. at 5 Hz. In a standard mechanical system, the dynamic response can shift by $1/2\pi$ rad. at the resonant frequency, therefore, the temporal accuracy of our system is acceptable to identifying the resonant characteristics.

3 EXPERIMENTAL METHOD

3.1 Protocol

The reflective markers were affixed to the ultrasound probe, the head, the sternum, the vibration exciter, and the floor. The head was selected for comparing with previous studies to see the validity of the proposed method. The sternum was selected to be compared with the stomach. These two are anatomically close to each other, meaning that this pair can be a good example to discuss the difference of the internal and external response of the human body. After stably placing the ultrasound probe on the abdomen so as to observe the stomach in the sagittal plane, ultrasound images and trajectories of the reflective markers were recorded while the seated subject was exposed to whole-body vibrations. In order to temporally align the ultrasound images with the optical tracker data, the ultrasound probe was given a step input both at the beginning and the end of the experiment.

Three kinds of input signals, frequency up-sweep, down-sweep, and white noise were introduced. The frequency of the frequency-sweep continuously ranged from 1 Hz to 10 Hz in the up-sweep, and from 10 Hz to 1 Hz in the down-sweep across a 15-second time span. The white noise signal contained frequency components from 1 Hz to 10 Hz with 15-second duration time. The frequency range was chosen so as to involve the first order natural frequency of the seated human body system [8, 11]. Two amplitudes, 1 m/s^2 r.m.s. and 2 m/s^2 r.m.s., were employed for each signal type. According to ISO2631-1 [37] vehicle comfort standards, the amplitudes are in the acceptable, yet uncomfortable range. The number of the input signals were totally six. Two seats, a flat-rigid seat made of acrylic sheets and a soft commercial seat, were introduced.

Table 1 shows the order of the trials. In order to understand how an empty versus full stomach impacts the dynamics, the subjects were asked to finish the meal at least four hours before the data collection to begin with an empty stomach. After a set of trials, the subjects were asked to drink 500 mL of water, then another set of trials ran with the filled stomach. The order for the input signal was randomized to eliminate the order effect. Each condition was iterated three times to see the repeatability. The start timing of sampling the ultrasound images were slightly changed every time, helping increase the number of images per cycle particularly for the higher frequency range. The total number of the trials were seventy two.

Three subjects shown in Table 2 participated in the experiment. The subjects were asked to sit on the seat mounted on the vibration exciter with standard upright posture and to maintain the initial posture while the vibrations were induced. Training was conducted in advance of the data collection to accustom the subjects to the vibrations. The experimental procedure and condition were approved by the Harvard University Institutional Review Board.

3.2 Data Processing

The dynamic responses of the head, the sternum, and the stomach as well as the displacement of the vibration exciter were identified with the method described in Section 2.2. These were all represented in the absolute coordinate system. The frequency response function (FRF) of each body part about Z-direction $F_{part,Z}(\omega)$ and X-direction $F_{part,X}(\omega)$ over the vertical displacement of the vibration exciter (ve)

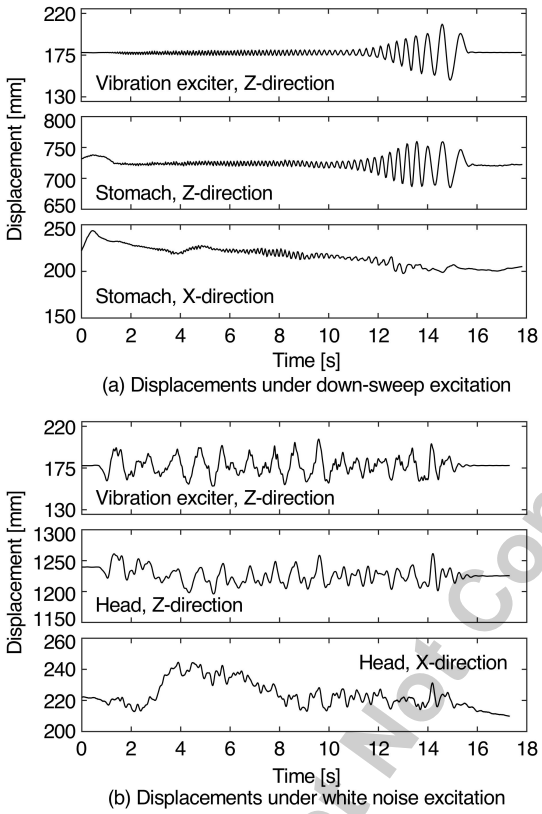

Fig. 7. Representative trajectories of the dynamic responses.

were calculated as transfer functions defined as

$$F_{part,Z}(\omega) = \frac{D^a_{part,Z}(\omega)}{D^a_{ve,Z}(\omega)}$$
$$F_{part,X}(\omega) = \frac{D^a_{part,X}(\omega)}{D^a_{ve,Z}(\omega)} \quad (3)$$

where D is the Fourier transform of d, and ω is a frequency. For time series analysis, $d^a_{part,Z}$ and $d^a_{part,X}$ were the Z- and X-directional components of the time series values of $\boldsymbol{d}^a_{part}$, respectively.

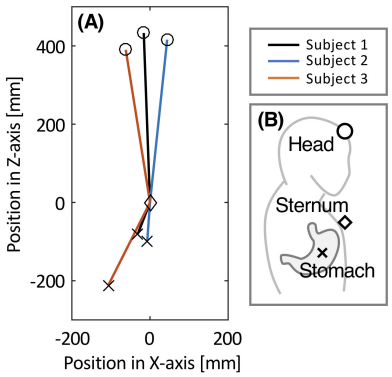

Fig. 8. Representative inter-subject variability of the seating posture. (A)Measured posture, (B)Corresponding points on the body.

3.3 Parametric Modeling

Based on the measured dynamic responses, the dynamics of each body part was modeled with Auto-regressive exogeneous model defined as

$$A(q)d^a_{part,XorZ} = B(q)d^a_{ve,Z} + e(t) \tag{4}$$

where q is the delay operator, t is time, and e is white-noise disturbance value. $A(q)$ and $B(q)$ were the coefficients defined as

$$\begin{aligned} A(q) &= 1 + a_1 q^{-1} + \cdots + a_{n_a} q^{-n_a} \\ B(q) &= b_0 + b_1 q^{-1} + \cdots + b_{n_b} q^{-n_b} \end{aligned} \tag{5}$$

where n_a and n_b are the number of poles and zeros, respectively. By converting the model to the continuous-time system, the model was transformed into the Laplace domain.

$$\bar{F}(s) = \frac{B(s)}{A(s)} \tag{6}$$

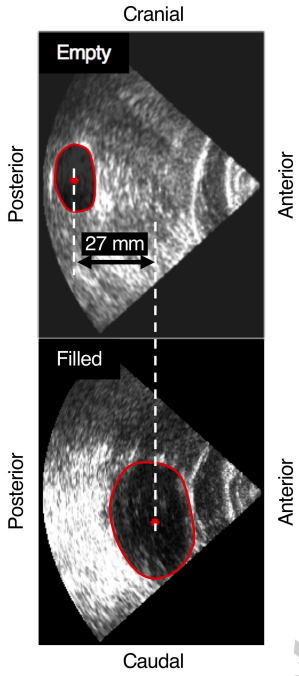

Fig. 9. Comparison of the representative imaged stomach under the empty and the filled condition.

where s is Laplace variable. The parameters of $A(s)$ and $B(s)$ were calculated by minimizing the root mean square error cost function J with the gradient descent method.

$$J = \left(\frac{1}{n} \sum_{i=n_l}^{n_l+n-1} (F(i) - \hat{F}(i))^2 \right)^{\frac{1}{2}} \tag{7}$$

where $\hat{F}$ is the frequency response function of $\bar{F}$, n_l indicates the minimum argument greater than 1 Hz, n is the number of data in the frequency range from 1 to 10 Hz.

4 RESULTS

4.1 Raw Data

Figure 7 shows representative trajectories of the dynamic responses measured with the proposed method. Figure 7 (a) compares the dynamic responses of the stomach with the vertical displacement of the vibration exciter under down-sweep excitation. Figure 7 (b) compares the dynamic responses of the head with the vertical displacement of the vibration exciter under white noise excitation.

Figure 8 shows representative inter-subject variability of the seating posture. Relative positions of the

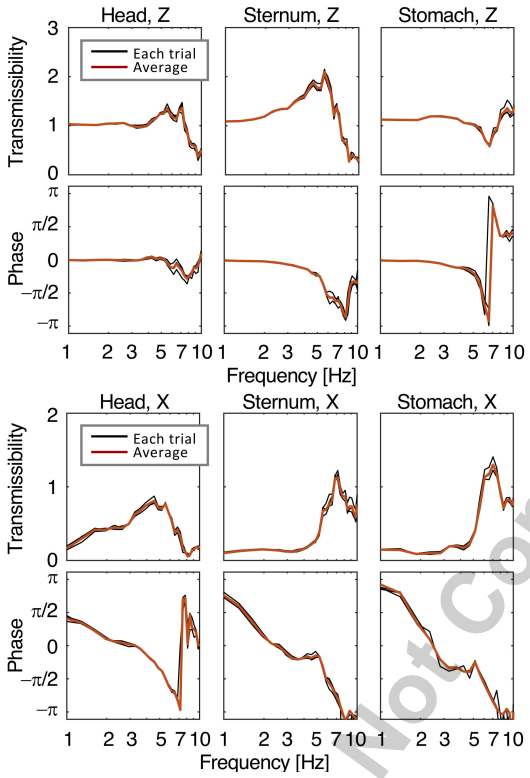

Fig. 10. Repeatability of the identified body dynamics. Red lines show average of all trials, black traces show FRFs for each individual trial. Upper: Vertical direction, Lower: Fore-and-aft direction.

head and the stomach centroid to the sternum in the sagittal plane were visualized.

Figure 9 shows comparison of the representative size and position of the stomach under the empty and the filled conditions.

4.2 Frequency Response Functions

4.2.1 Bode Diagrams

Figure 10 shows the repeatability of the identified body dynamics. Transmissibility was defined as the absolute value of F and phase was defined as the angle of F, respectively. The combination of the conditions - the white noise excitation, the 1 m/s^2 r.m.s. of the excitation amplitude, the rigid seat, and the empty stomach - was defined as the base condition. The dynamics both in the vertical Z-direction $F_{head,Z}$, $F_{sternum,Z}$, and $F_{stomach,Z}$ and the fore-and-aft X-direction $F_{head,X}$, $F_{sternum,X}$, and $F_{stomach,X}$ under the base condition were shown as a representative example. The results of the subject 1 were chosen here due to the median BMI value.

Figure 11 shows inter-subject variability at the base condition. The upper half is the dynamics in Z-

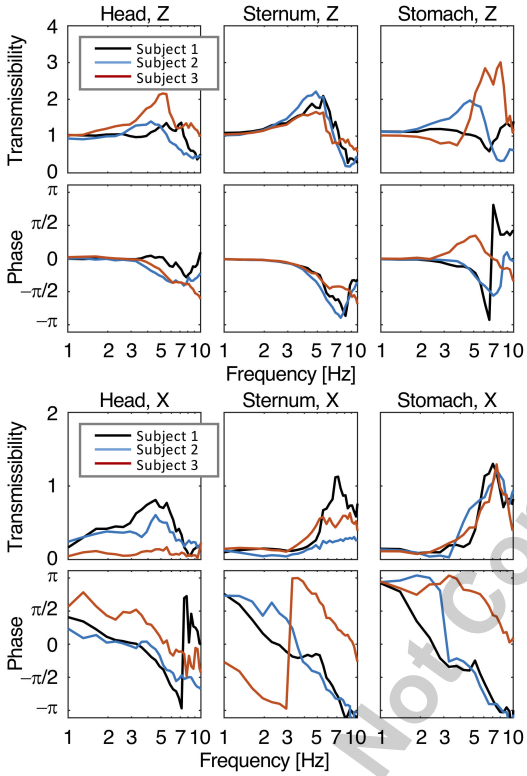

Fig. 11. Representative inter-subject variability. Black, blue, and red lines show results of subject 1, 2, and 3, respectively. Upper: Vertical direction, Lower: Fore-and-aft direction.

direction, and the lower half is those in X-direction. Figure 12 shows intra-subject variabilities caused by the experimental conditions. The top-left is the excitation pattern dependency, the top-right is the excitation amplitude dependency, the bottom-left is the seat compliance dependency, and the bottom-right is the stomach filling dependency, respectively. The undesignated conditions are the same as the base condition. The results of the subject 1 are chosen due to the median BMI value. Similarly to Fig. 11, the upper is the dynamics in Z-direction, and the lower is those in X-direction.

4.2.2 Parametric Models

Figure 13 shows the relationship between the model order and the fitting quality. The values of J are averages of all conditions and all subjects.

By setting 0.02 as the threshold of J to judge the fitting quality, fourth and eighth order were chosen as the minimum order to represent the experimentally identified body dynamics for the Z-direction and X-direction, respectively. Figure 14 shows the result of the parametric modeling about the base condition and the subject 1.

Figure 15 shows the loci of the poles about the Z-directional dynamics of the subject 1. Since the order of the model is fourth, two complex conjugate poles are obtained for each model. Only the poles having smaller absolute value and positive imaginary part are shown here as representative examples. Similarly to Fig. 12, intra-subject variabilities caused by the excitation pattern, the excitation amplitude, the seat compliance, and the stomach filling about the subject 1 are illustrated.

5 DISCUSSION

5.1 Quality of the Experimental Identification

The spatial and temporal accuracy described in the section 2.4 suggest that the developed system is sufficient to identify the FRF under 10 Hz of frequency with the input levels introduced here. The maximum spatial root mean square error of 0.224 mm is equivalent to the pixel size in the ultrasound image. The pixel size generally depends on the penetration depth of the ultrasound wave. In the setup reported here, the penetration depth was 100 mm, resulting in the good spatial accuracy. Theoretically, the angular accuracy of the ultrasound image plane can be improved with a larger tracking attachment for the ultrasound probe allowing to place reflective markers farther apart. In this study, the largest distance between two reflective markers was 70 mm and the spatial accuracy in resolving the position of reflective markers is 0.240 mm [36], suggesting approximately 0.4 deg of angular accuracy. The temporal absolute mean error of 13 ms is less than the refresh time of the ultrasound image of 33 ms, suggesting that the method to synchronize the ultrasound images and the optical tracker data works well. As shown in Fig. 7, the correlations between the vibration exciter displacement and the dynamic response of the body in Z-direction are high. The high correlation was also confirmed by calculating the cross correlation function at the calculation of FRF. The high correlation also supports the sufficiency of the accuracy because it proves that corresponding responses of each body part to input excitation were successfully measured.

The system reported here characterizes the dynamics of the seated human body. Particularly, the dynamics of the stomach under seated condition could be identified, whereas experimental previous studies have focused only on the dynamics observed at the skin surface as discussed in section 1.2. Good repeatability is shown in Fig. 10. The degree of deviation of the FRF in each trial from the average is considerably smaller than the inter- and intra-subject variabilities shown in Fig. 11 and Fig. 12, suggesting that the developed system can identify the subject-specific and condition-dependent FRF. The measured dynamic response of the body can include involuntary human motion, for instance, respiration and muscle movement. The excellent repeatability achieved by our system (Fig. 10) indicates that the unexpected

passive motion of the ultrasound probe can be compensated using the optical tracking system. Ambiguousness and unexpected artifacts in the ultrasound image generally degrade the accuracy of feature tracking. In order to smooth the raw ultrasound images, Gaussian filtering was taken at the beginning of the image processing. The active contour model was introduced to identify the centroid of the stomach. The method started with extracting the overall shape of the stomach, which the local aspects of the image cannot greatly affect in the image processing. The good repeatability can support the advantage of the proposed image processing method.

The system tracks displacement of each body part. Since the displacement becomes lower as frequency increases with a constant level of acceleration, it is difficult to identify FRF over 10 Hz of frequency with the high accuracy and repeatability. Better spatial resolution and higher sampling frequency of the ultrasound image will be required to track the dynamic response in higher frequency ranges.

5.2 Inter-subject variability

The large inter-subject variability in FRF is clearly visible in Fig. 11. Though the inter-subject variability in the vertical dynamics of the sternum is relatively small, those of other body parts and in different axis are significant. Moreover, the FRFs of subject 1 and 2 are roughly similar to each other, however, that of the subject 3 is different. A main reason for this variability is likely the difference in body habitus. The value of BMI of the subject 3 was much lower than the other two subjects. Another reason may be individual differences in posture. As shown in Fig. 8, the relative positions of the head and the stomach to the sternum vary with the subject. Subjects 1 and 2 appear to be slightly slouching, while subject 3 has chest forward. In addition to posture, the vertical position of the stomach of the subject 3 is more than 100 mm lower comparing to the other subjects.

These preliminary results demonstrate that the measurement system can identify subject-specific body dynamics. They also show a wide range of identified dynamics even across small sample population. Further experiments will be required to clarify the dependency of the body dynamics on body habitus, posture, age, gender and so on. This system can enable studies with many experimental subjects to fully characterize population characteristics.

5.3 Intra-subject variability

These results show that the excitation pattern impacts body dynamics as shown in Fig. 12. Generally, the amplitudes of the transmissibility under white noise excitation are smaller than those under up-sweep

and down-sweep excitation. Subjects reported that they tended to tense up while the white noise signal was induced. On the other hand, they reported that they could relax when the frequency-sweep signal was induced because the signal pattern was predictable. They also tensed up against the large displacement of the seat at low frequencies even under the frequency-sweep excitation. However, since the peak frequencies of the FRFs are over 5 Hz, the subjects could relax under the small displacement excitation in high frequency range. This variability of the subject response is the reason that white noise excitation was chosen as the base condition. The pole loci of the sternum and the stomach show only minor differences between the white noise and the up-sweep excitation as shown in Fig. 15. In contrast, the magnitude of the pole of the head under the white noise excitation is greater than that under the up-sweep excitation, suggesting that tensions of the muscles above the chest, probably the neck muscles, increase during white noise excitation.

The results also show a variation in measured body dynamics with excitation amplitude. The peak frequencies of the FRF at all body parts observed in this study become lower as the excitation amplitude increases. The magnitudes of the poles are also lower in all body parts under the amplitude of 2 m/s^2 r.m.s., suggesting that the balance between the effective mass and spring within the system can be changed with the excitation amplitude. The difference of the effective mass and spring of the seat-passenger system may be one of the reasons for the variability. Material nonlinearity of human soft tissue in stress-strain relationship can be another reason of the nonlinearity indicated by the amplitude dependency. Since the data collections were performed under the steady state, and the system was linearized at the equilibrium point, the material nonlinearity can impact on apparent stiffness of the system. The excitation amplitude dependency has been reported in previous studies [5–8, 11–13] of the head. It is shown here that a similar phenomenon may apply to the stomach.

The FRFs and the pole loci under the soft seat are quite different from those under the rigid seat. Soft seat compliance enables resonant behavior, resulting in higher magnitudes and lower peak frequencies of the FRFs under the soft seat. The pole loci suggest that the seat compliance impacts only the natural frequency of the system without significantly changing the damping factors, supporting the conclusion that the static compliance of the seat affects the FRF of the overall system. In previous studies, body dynamics have been experimentally identified with a rigid flat seat in order to eliminate the complicated nonlinearity of the soft seat made with foam rubber (typically urethane) material. ISO 2631 [37] suggests an experimental method to identify the FRF, and a weighting function to compensate the nonlinearity of human perception about the whole-body vibration. The weighting function seems to be derived from the experiments using

a rigid seat, therefore, it is implied that the seat compliance dependency should be taken into account in designing soft seats and vehicle suspension systems.

Stomach filling can impact body dynamics not only of the stomach but also of the head and the stomach. The vertical transmissibility at the stomach is slightly damped by drinking 500 mL of water as shown in Fig. 12. On the other hand, the vertical transmissibility of the head and the sternum are amplified, and the peak frequencies of the FRFs in the X-direction are lower in the filled condition. One cause of the variability can be attributed to the change in the size and the position of the stomach shown in Fig. 9. The 500 mL of water more than doubles the diameter of the stomach. In addition, the position of the stomach in the anterior-posterior direction is shifted 27 mm forward. The results suggest that stomach filling can affect not only the effective mass of the system but also the posture including the internal configuration, indicating that dynamic response of the internal soft tissue plays an important role in overall body dynamics.

5.4 Application

The peaks of magnitude and the phase delays observed in the FRFs suggest that the seat-passenger coupled system has resonance characteristics. However, the resonance characteristics are different in various locations in the body, implying that the observed resonance characteristics were caused by local structures and mechanical properties in addition to whole-body structure. The knowledge can be utilized for vehicular design because modulating the dynamic response of the body is a promising way to improve passenger comfort. Moreover, body dynamics including that of the stomach can greatly vary between individuals. Though further experiments will be required to fully characterize body dynamics with diverse metrics, the subject-specific body dynamics measured here can be utilized for adaptive adjustment of suspension control to each passenger. This kind of technology could be useful in providing more comfortable riding experience in shared vehicles.

The experimentally identified body dynamics can also be utilized for validating a computational human body model. In automotive engineering, computational models of passengers have been studied to predict vehicular ride comfort in the early stages of automobile design [38]. Distribution of contact pressure between the seat cushion and the passenger's anatomy have been well validated. However, conventional modeling studies did not focus on the dynamic response of soft tissues inside the passenger's body, thus the relationship between dynamics and subjective comfort are yet to be clarified. A related application is in surgical planning, where subject-specific computational models based on medical images can be used for preoperative surgical planning and training. The static configuration of internal organs has been modeled

in previous work [39], but the dynamic response of the soft tissue, including contact condition between adjacent tissues, are not well characterized. The method presented here to characterize the *in vivo* dynamics of internal soft tissue can be a breakthrough to improve the fidelity of several kinds of computational human body model.

6 CONCLUSION

The experimental system presented here has been shown to be an effective means to characterize the dynamics of internal soft tissue under whole-body vibration. The system comprises an ultrasound imaging system, a vibration exciter, and an optical tracker to identify *in-vivo* soft tissue dynamics as a frequency response function. In addition to the system design, data processing methods, and validation of the system, these results demonstrate that the dynamics of the stomach, a soft internal organ, are different from the dynamics observed at the skin surface for the head and the sternum. The system can further identify subject-specific and condition-dependent body dynamics. Further experiments will be conducted to associate the body dynamics with other body metrics. The identified body dynamics can be utilized for vehicular design as well as for developing a computational human body model for medical applications.

ACKNOWLEDGEMENTS

This work was supported by Toyota Motor North America, Inc.

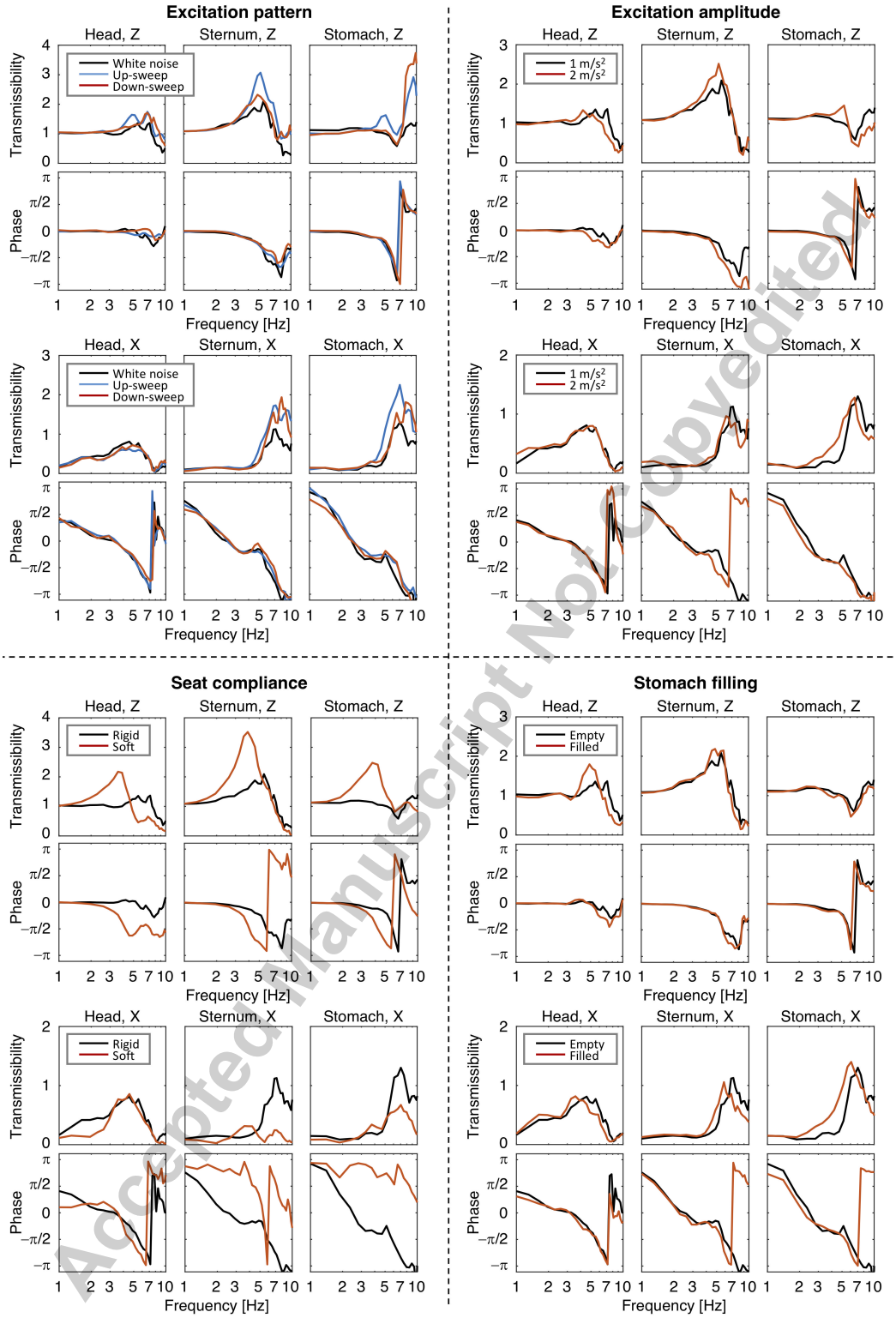

Fig. 12. Intra-subject variability of the subject 1 (median BMI). Top-left: Excitation pattern dependency, Top-right: Excitation amplitude dependency, Bottom-left: Seat compliance dependency, Bottom-right: Stomach filling dependency.

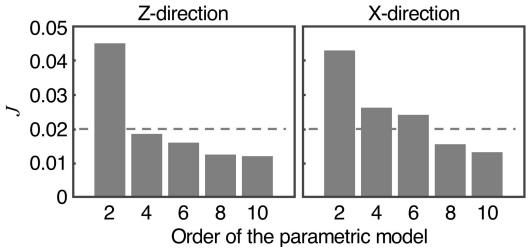

Fig. 13. Relationship between the model order and the fitting quality.

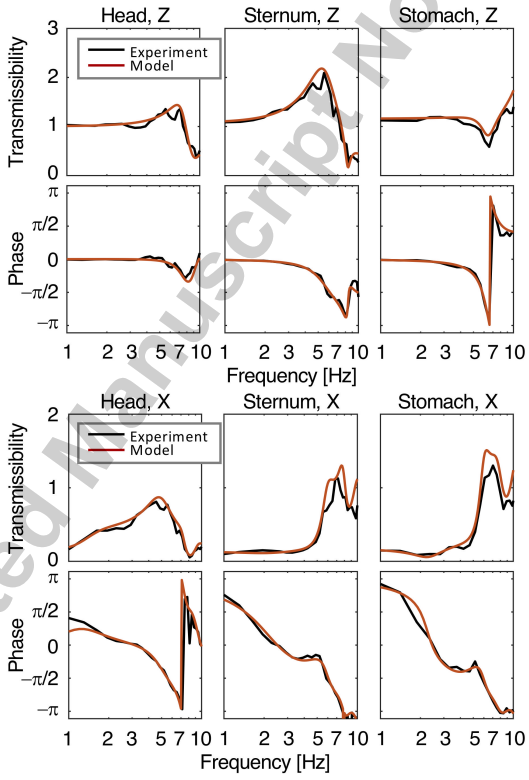

Fig. 14. Result of the parametric modeling about the subject 1 (median BMI). Upper: Vertical direction, Lower: Fore-and-aft direction.

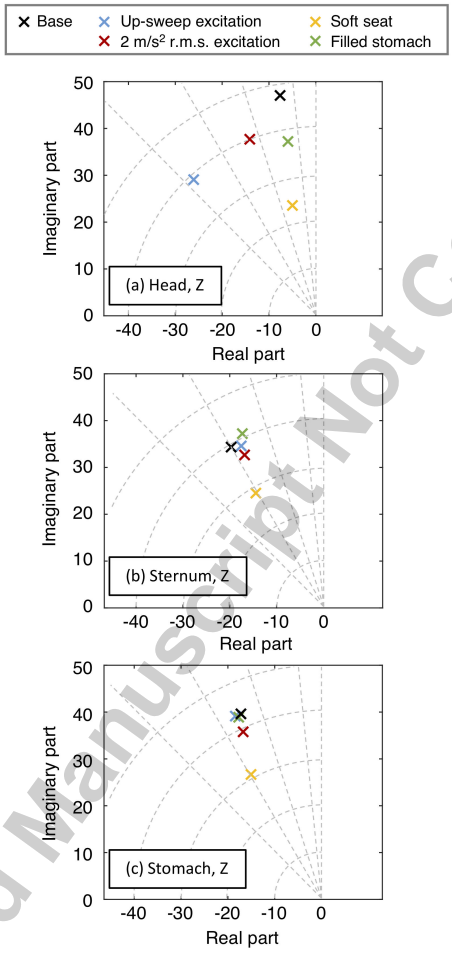

Fig. 15. Loci of poles from the model of the subject 1 (median BMI).

REFERENCES

[1] F. Schmäl, 2013. "Neuronal mechanisms and the treatment of motion sickness". *Pharmacology,* **91**(3-4), April, pp. 229–241. DOI:10.1159/000350185.

[2] W. J. Oosterveld, 1995. "Motion sickness". *Journal of Travel Medicine,* **2**(3), September, pp. 182–185.

[3] M. J. Griffin, 1990. *Handbook of Human Vibration*. Academic Press, Cambridge, MA. DOI:10.1016/C2009-0-02730-5.

[4] R. R. Coermann, 1962. "The mechanical impedance of the human body in sitting and standing position at low frequencies". *Human factors,* **4**(5), October, pp. 227–253. DOI:10.1177/001872086200400502.

[5] Z. Zhou and M. J. Griffin, 2014. "Response of the seated human body to whole-body vertical vibration: biodynamic responses to sinusoidal and random vibration". *Ergonomics,* **57**(5), April, pp. 693–713. DOI:10.1080/00140139.2014.898798.

[6] N. Nawayseh and M. J. Griffin, 2003. "Non-linear dual-axis biodynamic response to vertical whole-body vibration". *Journal of Sound and Vibration,* **268**(3), November, pp. 503–523. DOI:10.1016/S0022-460X(03)00254-2.

[7] Y. Matsumoto and M. J. Griffin, 2002. "Non-linear characteristics in the dynamic responses of seated subjects exposed to vertical whole-body vibration". *Journal of Biomechanical Engineering,* **124**(5), October, pp. 527–532. DOI:10.1115/1.1499959.

[8] N. J. Mansfield, P. Holmlund, R. Lundström, P. Lenzuni, and P. Nataletti, 2006. "Effect of vibration magnitude, vibration spectrum and muscle tension on apparent mass and cross axis transfer functions during whole-body vibration exposure". *Journal of Biomechanics,* **39**, December, pp. 3062–3070. DOI:10.1016/j.jbiomech.2005.09.024.

[9] C. Liu, Y. Qiu, and M. J. Griffin, 2017. "Dynamic forces over the interface between a seated human body and a rigid seat during vertical whole-body vibration". *Journal of Biomechanics,* **61**, August, pp. 176–182. DOI:10.1016/j.jbiomech.2017.07.015.

[10] C. L. Zimmermann and T. M. Cook, 1997. "Effects of vibration frequency and postural changes on human responses to seated whole-body vibration exposure". *International Archives of Occupational and Environmental Health,* **69**(3), January, pp. 167–179.

[11] T. E. Fairley and M. J. Griffin, 1989. "The apparent mass of the seated human body: vertical vibration". *Journal of Biomechanics,* **22**(2), pp. 81–94. DOI:10.1016/0021-9290(89)90031-6.

[12] N. J. Mansfield and M. J. Griffin, 1998. "Effect of magnitude of vertical whole-body vibration on absorbed power for the seated human body". *Journal of Sound and Vibration,* **215**(4), August, pp. 813–

825. DOI:10.1006/jsvi.1998.1596.

[13] S. D. Smith, 1994. "Nonlinear resonance behavior in the human exposed to whole-body vibration". *Shock and Vibration,* **1**(5), pp. 439–450. DOI:10.3233/SAV-1994-1504.

[14] E. B. Magid, R. R. Coermann, and G. H. Ziegenruecker, 1962. "Human tolerance to whole body sinusoidal vibration". *Aerospace medicine,* **31**(11), November, pp. 915–924.

[15] A. J. Jones and D. J. Saunders, 1972. "Equal comfort contours for whole body vertical, pulsed sinusoidal vibration". *Journal of Sound and Vibration,* **23**(1), July, pp. 1–14. DOI:10.1016/0022-460X(72)90785-7.

[16] B. Basri and M. J. Griffin, 2003. "Predicting discomfort from whole-body vertical vibration when sitting with an inclined backrest". *Applied Ergonomics,* **44**(3), May, pp. 423–434. DOI:10.1016/j.apergo.2012.10.006.

[17] Z. Zhou and M. J. Griffin, 2017. "Response of the seated human body to whole-body vertical vibration: discomfort caused by mechanical shocks". *Ergonomics,* **60**(3), March, pp. 347–357. DOI:10.1080/00140139.2016.1164902.

[18] Y. Huang and M. J. Griffin, 2014. "The discomfort produced by noise and whole-body vertical vibration presented separately and in combination". *Ergonomics,* **57**(11), November, pp. 1724–1738. DOI:10.1080/00140139.2014.943683.

[19] M. Bovenzi and C.T. J. Hulshof, 1999. "An updated review of epidemiologic studies on the relationship between exposure to whole-body vibration and low back pain (1986-1997)". *International Archives of Occupational and Environmental Health,* **72**(6), September, pp. 351–365. DOI:10.1007/s004200050387.

[20] R. R. Coermann, G. H. Ziegenruecker, A. L. Wittwer, and H. E. Von Gierke, 1960. "The passive dynamic mechanical properties of the human thorax-abdomen system and of the whole body system". *Aerospace Medicine,* **31**(6), June, pp. 227–253.

[21] R. Muksian and C. D. Nash Jr., 1974. "A model for the response of seated humans to sinusoidal displacements of the seat". *Journal of Biomechanics,* **7**, pp. 209–215.

[22] C. C. Liang and C. F. Chiang, 2008. "Modeling of a seated human body exposed to vertical vibrations in various automotive postures". *Industrial Health,* **46**(2), April, pp. 125–137. DOI:10.2486/indhealth.46.125.

[23] G. Tamaoki, T. Yoshimura, K. Kuriyama, and K. Nakai, 2008. "Modeling of spinal column of seated human body under exposure to whole-body vibration". *Journal of System Design and Dynamics,* **2**(6),

December, pp. 1327–1338. DOI:10.1299/jsdd.2.1327.

[24] Y. Matsumoto and M. J. Griffin, 2001. "Modelling the dynamic mechanisms associated with the principal resonance of the seated human body". *Clinical Biomechanics,* **16**(Supplement 1), pp. S31–S34. DOI:10.1016/S0268-0033(00)00099-1.

[25] T. Yoshimura, K. Nakai, and G. Tamaoki, 2005. "Multi-body dynamics modelling of seated human body under exposure to whole-body vibration". *Industrial Health,* **43**(3), May, pp. 441–447. DOI:10.2486/indhealth.43.441.

[26] G. Joshi, A. K. Bajaj, and P. Davies, 2010. "Whole-body vibratory response study using a nonlinear multi-body model of seat-occupant system with viscoelastic flexible polyurethane foam". *Industrial Health,* **48**(5), September, pp. 663–674. DOI:10.2486/indhealth.MSWBVI-13.

[27] S. Kitazaki and M. J. Griffin, 1997. "A model analysys of whole-body vertical vibration, using a finite element model of the human body". *Journal of Sound and Vibration,* **200**(1), February, pp. 83–103. DOI:10.1006/jsvi.1996.0674.

[28] Mikic, I., Krucinski, S., and Thomas, J. D., 1998. "Segmentation and tracking in echocardiographic sequences: Active contours guided by optical flow estimates". *IEEE transactions on medical imaging,* **17**(2), April, pp. 274–284. DOI:10.1109/42.700739.

[29] Luca, V. D., Székely, G., and Tanner, C., 2015. "Estimation of large-scale organ motion in b-mode ultrasound image sequences: A survey". *Ultrasound in medicine & biology,* **41**(12), December, pp. 3044–3062. DOI:10.1016/j.ultrasmedbio.2015.07.022.

[30] T. F. Chan and L. A. Vese, 2001. "Active contours without edges". *IEEE Transactions on Image Processing,* **10**(2), February, pp. 266–277. DOI:10.1109/83.902291.

[31] M. Kass, A. Witkin, and D. Terzopoulos, 1988. "Snakes: Active contour models". *International Journal of Computer Vision,* **1**(4), January, pp. 321–331. DOI:10.1007/BF00133570.

[32] A. Lasso, T. Heffter, A. Rankin, C. Pinter, T. Ungi and G. Fichtinger, 2014. "Plus: Open-source toolkit for ultrasound-guided intervention systems". *IEEE Transaction on Biomedical Engineering,* **61**(10), October, pp. 2527–2537. DOI:10.1109/TBME.2014.2322864.

[33] Bruder, R., Griese, F., Ernst, F., and Schweikard, A., 2011. "High-accuracy ultrasound target localization for hand-eye calibration between optical tracking systems and three-dimensional ultrasound". *Informatik aktuell*, January, pp. 179–183. DOI:10.1007/978-3-642-19335-4_38.

[34] Marinetto, E., García-Mato, D., García, A., Martínez, S., Desco, M., and Pascau, J., 2018. "Multicamera optical tracker assessment for computer aided surgery applications". *IEEE Access,* **6**, October,

pp. 64359–64370. DOI:10.1109/ACCESS.2018.2878323.

[35] Elfring, R., de la Fuente, M., and Radermacher, K., 2010. "Assessment of optical localizer accuracy for computer aided surgery systems". *Computer Aided Surgery,* **15**(1-3), pp. 1–12. DOI:10.3109/10929081003647239.

[36] Xiao, G., Bonmati, E., Thompson, S., Evans, J., Hipwell, J., Nikitichev, D., Gurusamy, K., Ourselin, S., Hawkes, D. J., Davidson, B., and Clarkson, M. J., 2018. "Electromagnetic tracking in image-guided laparoscopic surgery: Comparison with optical tracking and feasibility study of a combined laparoscope and laparoscopic ultrasound system". *Medical physics,* **45**(11), October, pp. 5094–5104. DOI:10.1002/mp.13210.

[37] ISO2631-1, 1997. "Mechanical vibration and shock - evaluation of human exposure to whole-body vibration, part 1: General requirements, 2nd ed.".

[38] A. Siefert, 2016. "Occupant comfort - a mixture of joint angles, seat pressure and tissue loads". *SAE Technical Paper*, April. Paper 2016-01-1438, DOI:10.4271/2016-01-1438.

[39] M. A. Scherer and D.A. Geller, 2015. *New preoperative images, surgical planning, and navigation. In: Fong Y., Giulianotti P., Lewis J., Groot Koerkamp B., Reiner T. (eds) Imaging and visualization in the modern operating room*. Springer, New York, NY. DOI:10.1007/978-1-4939-2326-7_16.

APPENDIX A: MODEL PARAMETERS

All values of zeros, poles and gain of the parametric models corresponding to Fig. 12 are listed in Table 3 and Table 4.

Table 3. Zeros, poles, and gain in the modeled vertical dynamics of the subject1 (median BMI).

Signal type Amplitude	Seat compliance Stomach filling	Body part Gain	Zeros Poles			
White Noise 1 m/s^2 r.m.s.	Rigid Empty	Head 6.36e-01	-49.88+ 97.69j -21.71+102.30j	-49.88- 97.69j -21.71-102.30j	-5.19+ 56.80j -7.62+ 47.00j	-5.19- 56.80j -7.62- 47.00j
Up-sweep 1 m/s^2 r.m.s.	Rigid Empty	Head 6.51e-01	-0.42+ 42.89j -1.08+ 42.36j	-0.42- 42.89j -1.08- 42.36j	-48.29+ 2.80j -26.12+ 29.14j	-48.29- 2.80j -26.12- 29.14j
White Noise 2 m/s^2 r.m.s.	Rigid Empty	Head 6.54e-01	-147.43+ 0.00j -60.71+ 75.81j	-4.34+ 58.55j -60.71- 75.81j	-4.34- 58.55j -14.08+ 37.76j	-43.05+ 0.00j -14.08- 37.76j
White Noise 1 m/s^2 r.m.s.	Soft Empty	Head 5.92e-02	-93.92+ 52.65j -3.83+ 41.54j	-93.92- 52.65j -3.83- 41.54j	-3.12+ 37.98j -4.95+ 23.61j	-3.12- 37.98j -4.95- 23.61j
White Noise 1 m/s^2 r.m.s.	Rigid Filled	Head 4.14e-01	-40.95+ 88.57j -15.39+ 98.71j	-40.95- 88.57j -15.39- 98.71j	-12.08+ 54.90j -5.99+ 37.27j	-12.08- 54.90j -5.99- 37.27j
White Noise 1 m/s^2 r.m.s.	Rigid Empty	Sternum 5.57e-02	-199.38+ 0.00j -4.82+ 51.25j	-119.23+ 0.00j -4.82- 51.25j	-0.99+ 52.51j -9.72+ 34.43j	-0.99- 52.51j -9.72- 34.43j
Up-sweep 1 m/s^2 r.m.s.	Rigid Empty	Sternum -1.36e-01	148.98+ 0.00j -4.13+ 60.35j	-75.13+ 0.00j -4.13- 60.35j	-7.53+ 57.13j -7.46+ 34.60j	-7.53- 57.13j -7.46- 34.60j
White Noise 2 m/s^2 r.m.s.	Rigid Empty	Sternum -1.49e-01	96.59+ 0.00j -4.04+ 52.28j	-75.51+ 0.00j -4.04- 52.28j	-2.87+ 53.48j -6.85+ 32.64j	-2.87- 53.48j -6.85- 32.64j
White Noise 1 m/s^2 r.m.s.	Soft Empty	Sternum -8.96e-03	317.00+ 0.00j -7.49+ 42.84j	-88.95+ 0.00j -7.49- 42.84j	-19.42+ 67.76j -4.41+ 24.58j	-19.42- 67.76j -4.41- 24.58j
White Noise 1 m/s^2 r.m.s.	Rigid Filled	Sternum 1.31e-01	-84.11+ 51.95j -14.84+ 43.13j	-84.11- 51.95j -14.84- 43.13j	-3.05+ 50.60j -7.30+ 37.17j	-3.05- 50.60j -7.30- 37.17j
White Noise 1 m/s^2 r.m.s.	Rigid Empty	Stomach 8.38e-01	-55.95+ 94.80j -0.72+ 94.25j	-55.95- 94.80j -0.72- 94.25j	4.50+ 40.25j -7.24+ 39.54j	4.50- 40.25j -7.24- 39.54j
Up-sweep 1 m/s^2 r.m.s.	Rigid Empty	Stomach 1.12e+00	-49.16+ 37.87j -14.93+ 61.67j	-49.16- 37.87j -14.93- 61.67j	8.18+ 39.83j -8.31+ 39.07j	8.18- 39.83j -8.31- 39.07j
White Noise 2 m/s^2 r.m.s.	Rigid Empty	Stomach 1.26e+00	-53.99+ 50.40j -40.52+ 79.88j	-53.99- 50.40j -40.52- 79.88j	5.84+ 40.84j -6.82+ 35.88j	5.84- 40.84j -6.82- 35.88j
White Noise 1 m/s^2 r.m.s.	Soft Empty	Stomach 2.15e-01	-67.35+ 48.05j -6.07+ 50.59j	-67.35- 48.05j -6.07- 50.59j	6.21+ 39.14j -5.16+ 26.77j	6.21- 39.14j -5.16- 26.77j
White Noise 1 m/s^2 r.m.s.	Rigid Filled	Stomach 9.80e-01	-58.01+ 90.85j -24.97+ 98.84j	-58.01- 90.85j -24.97- 98.84j	4.58+ 39.79j -7.79+ 38.91j	4.58- 39.79j -7.79- 38.91j

Table 4. Zeros, poles, and gain in the modeled fore-and-aft dynamics of the subject1 (median BMI).

Signal type Amplitude	Seat compliance Stomach filling	Body part Gain	Zeros Poles			
White Noise	Rigid	Head	-59.83+ 41.14j	-59.83- 41.14j	5.13+ 50.74j	5.13- 50.74j
			-3.68+ 51.03j	-3.68- 51.03j	-2.72+ 5.82j	-2.72- 5.82j
1 m/s^2 r.m.s.	Empty	7.58e-02	-5.53+ 58.48j	-5.53- 58.48j	-3.66+ 45.55j	-3.66- 45.55j
			-7.95+ 30.44j	-7.95- 30.44j	-4.29+ 8.19j	-4.29- 8.19j
Up-sweep	Rigid	Head	-58.53+ 41.48j	-58.53- 41.48j	-3.18+ 50.77j	-3.18- 50.77j
			6.46+ 48.36j	6.46- 48.36j	-10.06+ 0.00j	-1.19+ 0.00j
1 m/s^2 r.m.s.	Empty	6.34e-02	-4.05+ 58.74j	-4.05- 58.74j	-2.04+ 44.90j	-2.04- 44.90j
			-7.96+ 30.64j	-7.96- 30.64j	-6.84+ 8.77j	-6.84- 8.77j
White Noise	Rigid	Head	-229.59+ 0.00j	-110.02+ 0.00j	1.67+ 54.29j	1.67- 54.29j
			-8.10+ 43.75j	-8.10- 43.75j	-18.89+ 0.00j	1.25+ 0.00j
2 m/s^2 r.m.s.	Empty	1.29e-02	-6.69+ 60.62j	-6.69- 60.62j	-4.49+ 41.17j	-4.49- 41.17j
			-7.03+ 30.61j	-7.03- 30.61j	-8.20+ 6.94j	-8.20- 6.94j
White Noise	Soft	Head	-17.20+115.68j	-17.20-115.68j	-1.11+ 57.26j	-1.11- 57.26j
			-67.57+ 0.00j	-52.94+ 0.00j	-9.45+ 20.03j	-9.45- 20.03j
1 m/s^2 r.m.s.	Empty	3.22e-03	-1.97+ 58.08j	-1.97- 58.08j	-6.20+ 41.84j	-6.20- 41.84j
			-5.32+ 28.27j	-5.32- 28.27j	-3.59+ 21.67j	-3.59- 21.67j
White Noise	Rigid	Head	-63.07+ 0.00j	-4.00+ 60.70j	-4.00- 60.70j	0.52+ 47.03j
			0.52- 47.03j	-9.15+ 17.43j	-9.15- 17.43j	-3.43+ 0.00j
1 m/s^2 r.m.s.	Filled	9.87e-02	-2.02+ 60.94j	-2.02- 60.94j	-4.50+ 40.53j	-4.50- 40.53j
			-5.20+ 23.04j	-5.20- 23.04j	-6.76+ 11.00j	-6.76- 11.00j
White Noise	Rigid	Sternum	-675.22+ 0.00j	-89.66+ 0.00j	-4.67+ 52.68j	-4.67- 52.68j
			-8.97+ 29.27j	-8.97- 29.27j	6.84+ 11.83j	6.84- 11.83j
1 m/s^2 r.m.s.	Empty	-1.27e-02	-6.56+ 63.53j	-6.56- 63.53j	-3.59+ 49.24j	-3.59- 49.24j
			-4.11+ 36.87j	-4.11- 36.87j	-9.17+ 11.13j	-9.17- 11.13j
Up-sweep	Rigid	Sternum	101.98+ 0.00j	-77.93+ 0.00j	-0.30+ 51.62j	-0.30- 51.62j
			-4.54+ 23.98j	-4.54- 23.98j	4.77+ 11.91j	4.77- 11.91j
1 m/s^2 r.m.s.	Empty	5.28e-01	-30.19+ 62.69j	-30.19- 62.69j	-0.69+ 51.91j	-0.69- 51.91j
			-9.98+ 40.23j	-9.98- 40.23j	-8.42+ 16.46j	-8.42- 16.46j
White Noise	Rigid	Sternum	-94.64+ 0.00j	70.19+ 0.00j	-5.30+ 56.10j	-5.30- 56.10j
			-4.48+ 30.55j	-4.48- 30.55j	5.94+ 14.67j	5.94- 14.67j
2 m/s^2 r.m.s.	Empty	2.14e-01	-58.17+ 0.00j	-4.30+ 62.12j	-4.30- 62.12j	-7.57+ 43.48j
			-7.57- 43.48j	-3.74+ 32.34j	-3.74- 32.34j	-8.65+ 0.00j
White Noise	Soft	Sternum	82.21+ 0.00j	-71.78+ 0.00j	-0.67+ 62.18j	-0.67- 62.18j
			-1.08+ 34.70j	-1.08- 34.70j	-2.56+ 14.37j	-2.56- 14.37j
1 m/s^2 r.m.s.	Empty	1.71e-02	-0.98+ 61.63j	-0.98- 61.63j	-2.81+ 43.65j	-2.81- 43.65j
			-2.97+ 26.45j	-2.97- 26.45j	-4.17+ 16.70j	-4.17- 16.70j
White Noise	Rigid	Sternum	102.48+ 0.00j	-74.06+ 0.00j	-2.08+ 50.82j	-2.08- 50.82j
			-8.88+ 23.85j	-8.88- 23.85j	9.95+ 9.69j	9.95- 9.69j
1 m/s^2 r.m.s.	Filled	8.08e-02	-15.26+ 53.98j	-15.26- 53.98j	-2.48+ 50.54j	-2.48- 50.54j
			-3.83+ 35.06j	-3.83- 35.06j	-6.32+ 11.86j	-6.32- 11.86j
White Noise	Rigid	Stomach	-73.14+ 55.29j	-73.14- 55.29j	-7.49+ 53.94j	-7.49- 53.94j
			-7.46+ 31.56j	-7.46- 31.56j	1.94+ 14.02j	1.94- 14.02j
1 m/s^2 r.m.s.	Empty	-1.27e-01	-6.66+ 65.91j	-6.66- 65.91j	-5.99+ 48.17j	-5.99- 48.17j
			-3.61+ 37.35j	-3.61- 37.35j	-7.61+ 14.55j	-7.61- 14.55j
Up-sweep	Rigid	Stomach	-1.87+ 60.58j	-1.87- 60.58j	-54.83+ 0.00j	-1.24+ 37.56j
			-1.24- 37.56j	-24.94+ 0.00j	2.39+ 12.72j	2.39- 12.72j
1 m/s^2 r.m.s.	Empty	-4.69e-01	-0.90+ 60.83j	-0.90- 60.83j	-6.10+ 44.98j	-6.10- 44.98j
			-1.20+ 37.13j	-1.20- 37.13j	-15.29+ 10.84j	-15.29- 10.84j
White Noise	Rigid	Stomach	-57.61+ 0.00j	-2.56+ 60.63j	-2.56- 60.63j	-1.05+ 44.12j
			-1.05- 44.12j	-12.19+ 0.00j	3.00+ 11.19j	3.00- 11.19j
2 m/s^2 r.m.s.	Empty	-3.16e-01	-2.58+ 61.76j	-2.58- 61.76j	-0.60+ 43.88j	-0.60- 43.88j
			-7.63+ 38.56j	-7.63- 38.56j	-6.29+ 9.28j	-6.29- 9.28j
White Noise	Soft	Stomach	702.34+ 0.00j	-86.15+ 0.00j	-5.07+ 65.48j	-5.07- 65.48j
			-3.68+ 32.49j	-3.68- 32.49j	-1.57+ 13.95j	-1.57- 13.95j
1 m/s^2 r.m.s.	Empty	6.40e-03	-4.95+ 62.15j	-4.95- 62.15j	-8.74+ 45.42j	-8.74- 45.42j
			-3.85+ 33.76j	-3.85- 33.76j	-6.08+ 19.29j	-6.08- 19.29j
White Noise	Rigid	Stomach	-50.15+ 36.14j	-50.15- 36.14j	-0.70+ 46.99j	-0.70- 46.99j
			-13.49+ 42.21j	-13.49- 42.21j	4.12+ 10.58j	4.12- 10.58j
1 m/s^2 r.m.s.	Filled	-1.84e-01	-10.18+ 50.96j	-10.18- 50.96j	0.41+ 47.18j	0.41- 47.18j
			-4.00+ 37.17j	-4.00- 37.17j	-10.84+ 12.43j	-10.84- 12.43j

Figure list

Figure 1: System configuration. (A)Overall configuration, (B,C)Assembly of the TEE probe, the reflective markers, and the coupling, (D)Affixed TEE probe using two straps.

Figure 2: Coordinate transforms for resolving body part motions to the absolute fixed coordinate system, using head motion as an example.

Figure 3: Image processing pipeline for extracting the stomach centroid.

Figure 4: Coordinate transforms for resolving the stomach centroid into absolute coordinates.

Figure 5: String-based phantom for testing system accuracy. Strings are mounted at skew angles so inter-string distances as measured in the ultrasound images define unique image plane locations and orientations in phantom coordinates, following standard ultrasound calibration methods [32].

Figure 6: Validation result. (A)Vertical displacement of the reference and the cross point, (B) Spatial error.

Figure 7: Representative trajectories of the dynamic responses.

Figure 8: Representative inter-subject variability of the seating posture. (A)Measured posture, (B)Corresponding points on the body.

Figure 9: Comparison of the representative imaged stomach under the empty and the filled condition.

Figure 10: Repeatability of the identified body dynamics. Red lines show average of all trials, black traces show FRFs for each individual trial. Upper: Vertical direction, Lower: Fore-and-aft direction.

Figure 11: Representative inter-subject variability. Black, blue, and red lines show results of subject 1, 2, and 3, respectively. Upper: Vertical direction, Lower: Fore-and-aft direction.

Figure 12: Intra-subject variability of the subject 1 (median BMI). Top-left: Excitation pattern dependency, Top-right: Excitation amplitude dependency, Bottom-left: Seat compliance dependency, Bottom-right: Stomach filling dependency.

Figure 13: Relationship between the model order and the fitting quality.

Figure 14: Result of the parametric modeling about the subject 1 (median BMI). Upper: Vertical direction, Lower: Fore-and-aft direction.

Figure 15: Loci of poles from the model of the subject 1 (median BMI).

Table list

Table 1: Order of the trials.

Table 2: Information about the experimental subjects.

Table 3: Zeros, poles, and gain in the modeled vertical dynamics of the subject1 (median BMI).

Table 4: Zeros, poles, and gain in the modeled fore-and-aft dynamics of the subject1 (median BMI).